reactions

MDPI

Article

Cerium Oxide Nanoparticles for Efficient Photocatalytic Degradation of Red Amaranth Dye

Jhonathan Castillo-Saenz [1,2,*,†], Eduardo Estrada-Movilla [1,†], Benjamín Valdez-Salas [1,*], Ernesto Beltrán-Partida [1], Jorge Salvador-Carlos [1], Esneyder Puello-Polo [2] and Roberto Gamboa-Becerra [1]

[1] Core Facilities of Chemistry and Advanced Materials, Instituto de Ingeniería, Universidad Autónoma de Baja California, Blvd. Benito Juárez and Normal s/n, Mexicali 21280, Baja California, Mexico; eduardo.estrada.movilla@uabc.edu.mx (E.E.-M.); beltrane@uabc.edu.mx (E.B.-P.); jsalvador@uabc.edu.mx (J.S.-C.); roberto.gamboa@uabc.edu.mx (R.G.-B.)
[2] Grupo de Investigación en Oxi/Hidrotratamiento Catalítico y Nuevos Materiales, Programa de Química-Ciencias Básicas, Universidad del Atlántico, Barranquilla 080002, Colombia; esneyderpuello@mail.uniatlantico.edu.co
* Correspondence: jhonathan.saenz@uabc.edu.mx (J.C.-S.); benval@uabc.edu.mx (B.V.-S.)
† These authors contributed equally to this work.

Abstract

Red Amaranth (RA) Azo dye is a persistent pollutant in wastewater and stands as a toxicological risk, which has led to the development of effective methods for its removal and photocatalytic degradation. Therefore, CeO_2 nanoparticles were synthesized by a controlled precipitation method, and Ultraviolet-Visible (UV–Vis) analysis and Tauc plots yielded a band gap of ~3.24 eV. The CeO_2 nanoparticles showed the fluorite cubic phase, and nearly spherical particles with an average size of ~10 nm. Nitrogen physisorption revealed a type IV isotherm with a Brunauer–Emmett–Teller (BET) surface area of 85.27 $m^2 \cdot g^{-1}$ and a total pore volume of 0.27 $cm^3 \cdot g^{-1}$, indicating a mesoporous structure and high surface accessibility. The chemical behavior showed Ce and O, consistent with phase purity. Photocatalytic performance was evaluated in 20 ppm aqueous solution of RA under 365 nm UV irradiation (LED 100 W), with a temperature of ~20 °C and a 15 min dark adsorption step. Concentration decay was followed at λ_{max} = 520 nm by Lambert–Beer. The degradation efficiency η and pseudo-first-order kinetic were obtained from $\ln(C_0/C_t)$ vs. time. In addition, chemical oxygen demand (COD) tests were performed on RA solution before and after photodegradation, showing a COD reduction of ~85% (from 19.8 to 3 mg $O_2 \cdot L^{-1}$), which corroborates mineralization beyond chromophore bleaching. Under [C_0 = 20 mg·L^{-1}] and [m_{cat} = 1.0 g·L^{-1}], CeO_2 achieved [RA = 90% at 180 min, k = 0.0125 min^{-1}]. These results demonstrate that CeO_2 is an effective photocatalyst for RA degradation under UV-A irradiation, integrating adsorption, kinetic behavior, and mineralization performance into a coherent structure–property relationship.

Keywords: photocatalytic nanoparticles; photocatalysis; contaminated wastewater; environmental remediation

Received: 8 January 2026
Revised: 4 March 2026
Accepted: 25 March 2026
Published: 31 March 2026

1. Introduction

Azo dyes are among the most persistent classes of organic contaminants in textile effluents. Their high chemical stability, aqueous solubility, and sulfonated groups confer resistance to conventional treatment processes (coagulation–flocculation, adsorption, activated sludge), favoring their transport into water bodies and the formation of recalcitrant

aromatic byproducts [1,2]. Within this group, Red Amaranth (RA) stands out due to its azo (–N=N–) structure conjugated with sulfonated aromatic rings, which provides high chromatic intensity and remarkable resistance to biodegradation, thus posing environmental and toxicological challenges when evaluated only by spectral decolorization and not by mineralization [3,4].

Advanced Oxidation Processes (AOPs) represent an effective route for the degradation of such compounds, as they generate reactive oxygen species (ROS) capable of cleaving π bonds and opening aromatic rings [2,5]. Among AOPs, heterogeneous photocatalysis has been established as a versatile alternative owing to its potential for operation at room temperature, compatibility with complex matrices, and feasibility of coupling with UV/visible-light sources [2,6]. Upon irradiation, semiconductors generate e^-/h^+ pairs which, in the presence of O_2 and H_2O, yield ROS ($\bullet OH$, $\bullet O_2^-$, $HO_2\bullet$, H_2O_2) that drive oxidative attack [5,6]. However, overall efficiency depends critically on charge separation, substrate adsorption, and electron-transfer kinetics at the solid–liquid interface [7,8]. Well-established semiconductor photocatalysts such as TiO_2 and ZnO have been extensively investigated for azo dye degradation due to their strong oxidative capability and chemical stability [9,10]. Reported performances for these oxide systems typically show degradation efficiencies ranging from about 60% to nearly complete removal within irradiation times of approximately 80–120 min, depending on catalyst composition and reaction conditions [9,10]. Recent studies have further optimized their structural and optical properties to enhance photocatalytic efficiency [9,10]. However, persistent challenges remain, including rapid electron–hole recombination, limited visible-light response, and restricted oxygen activation pathways, which constrain overall mineralization efficiency [11]. These limitations highlight the need for alternative oxide systems with tunable defect chemistry and redox flexibility.

In this context, cerium dioxide (CeO_2) has emerged as a promising photocatalyst due to its fluorite structure, the Ce^{4+}/Ce^{3+} redox couple, and the presence of oxygen vacancies (V_O), which act as trapping/transfer centers, reducing recombination and enhancing O_2 activation [1,6,7]. At the nanoscale, CeO_2 nanoparticles (NPs) exhibit a higher surface fraction of defects, a larger specific area, and the ability to tune the Ce^{3+}/Ce^{4+} ratio. These features correlate with a higher density of active sites and favorable redox dynamics for the sustained generation of ROS [5,7,12–15]. Additionally, the near-UV excitation threshold (E_g = ~3.0–3.2 eV) allows efficient activation under UV-A LED (365 nm), overcoming the practical limitations of mercury lamps (heating, safety, broad spectrum) and facilitating energy balance and scalability [13,14].

Despite advances with TiO_2, ZnO, and related heterostructures, the specific evidence for RA degradation over CeO_2 remains fragmented and heterogeneous: (i) experimental conditions vary widely (concentration, pH, catalyst dosage, irradiance), hindering comparisons [3,4,16–19]; (ii) UV–Vis decolorization is often reported as the sole indicator, omitting mineralization metrics (e.g., Chemical Oxygen Demand (COD) and Total Organic Carbon (TOC)) and the identification of released inorganic ions [8,12,13,20–22]; (iii) essential controls (photolysis, dark adsorption) are not always included, preventing isolation of the net photocatalytic effect [18,19]; and (iv) explicit mechanistic suggestions linking CeO_2 defect chemistry (Ce^{3+}/V_O) with azo bond cleavage and the evolution of aromatic intermediates into low-molecular-weight carboxylic acids and, ultimately, $CO_2 + H_2O$ are scarce [5,7,12]. To the best of our knowledge, only a limited number of reports have addressed RA degradation using CeO_2-based systems, with most studies focusing on other dyes under heterogeneous conditions, making direct comparisons difficult.

To address these gaps, this work reports the synthesis of CeO_2 nanoparticles via a controlled precipitation route and their evaluation in the photocatalytic degradation of

Red Amaranth under UV-A LED irradiation (365 nm, 100 W), isothermal operation (~20 °C), and a 15 min dark adsorption pre-equilibrium with explicit photolysis controls. The primary objective is to establish a structure–property–activity relationship by correlating nanoscale features with adsorption behavior, kinetic performance, and mineralization trends. Degradation rates were determined using pseudo-first-order kinetics based on $\ln(C_0/C_t)$ vs. time, and COD analysis was employed to assess oxidation beyond chromophore decolorization.

2. Experimental Details

2.1. Synthesis of CeO_2 Nanoparticles

A 0.10 M cerium (III) precursor solution was prepared by dissolving 2.17 g of cerium (III) nitrate hexahydrate ($Ce(NO_3)_3 \cdot 6H_2O$, ≥99%, (Sigma Aldrich, St. Louis, MO, USA)) in 50 mL of deionized water (18.0 MΩ·cm) at room temperature under magnetic stirring at 300 rpm. The pH was adjusted to 10.0 by the dropwise addition of NaOH solution at 1.0 M with continuous stirring. The resulting $Ce(OH)_3$ precipitate was allowed to mature for 30 min to homogenize the precipitate and minimize local pH gradients prior to filtration, contributing to improved particle uniformity after calcination, and was then recovered by vacuum filtration (Polytetrafluoroethylene (PTFE) membrane, 0.45 µm), thoroughly washed with deionized water followed by ethanol, and dried at 90 °C for 24 h. The dried hydroxide was calcined in air at 500 °C for 2 h using a muffle furnace with a heating ramp of 10 °C·min^{-1} and natural cooling inside the furnace to obtain CeO_2 nanoparticles (Figure 1).

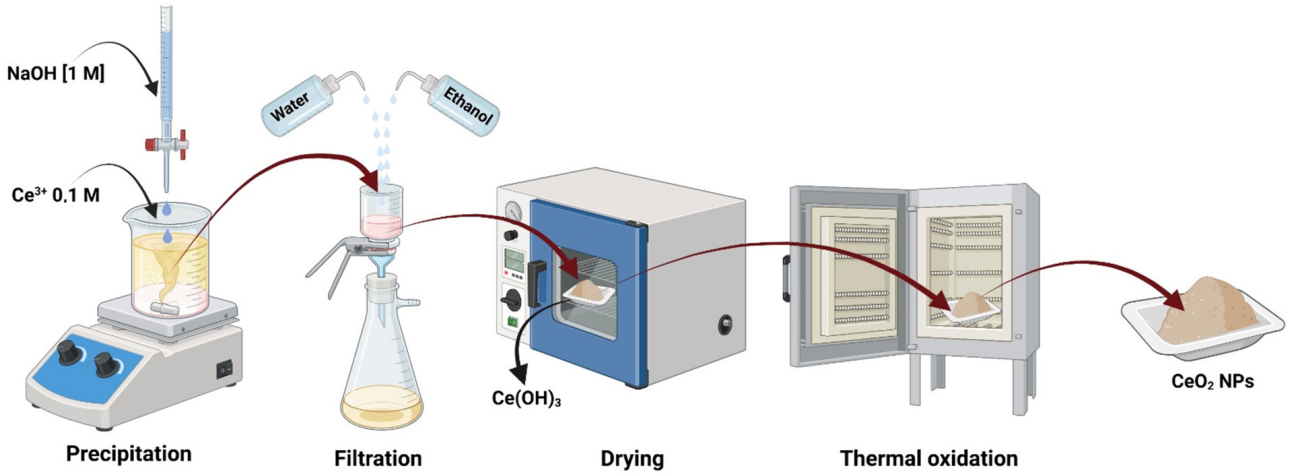

Figure 1. Flowchart for the synthesis of CeO_2 by the precipitation method.

2.2. CeO_2 Nanoparticles Characterization

The optical band gap of CeO_2 was measured by UV–Vis spectroscopy (Shimadzu UV-260, Shimadzu Corporation, Kyoto, Japan). The morphology and particle size were examined by High-Resolution Transmission Electron Microscopy (HR-TEM JEM-2010, 200 kV; JEOL, Akishima, Japan). Elemental composition was assessed by Energy-Dispersive X-ray Spectroscopy (EDS) using a Field-Emission Scanning Electron Microscope (FE-SEM) Lyra 3 XMU, Tescan, Brno, Czech Republic) equipped with a Bruker Quantax X-Flash 6160 detector. Structural and crystallographic information was obtained by HR-TEM and X-ray diffraction (XRD; PANalytical Empyrean, Almelo, The Netherlands), Cu Kα, λ = 0.15406 nm) with an X'Celerator detector, scanning 2θ = 20–90° at room temperature. Textural properties were evaluated by N_2 adsorption–desorption isotherms at 77 K using a TriStar II Plus surface area and porosity analyzer (Micromeritics, Norcross, GA, USA).

2.3. Photocatalytic Degradation Test

Photocatalytic experiments were conducted in a 50 mL batch reactor using a 365 nm UV-LED source (100 W). The photocatalytic reactor setup used in this study is shown in Figure S1 (Supplementary Materials). The irradiance at the reactor surface was not directly measured; therefore, kinetic parameters are reported under specific operating conditions without normalization to photon flux. A 20 ppm aqueous solution of Red Amaranth was prepared, and 50 mg of CeO_2 was added (equivalent to 1.0 $g \cdot L^{-1}$). This catalyst loading was selected to enable a comparison with commonly reported conditions in heterogeneous photocatalysis of azo dyes. A detailed mass-transfer analysis was beyond the scope of the present study. Suspensions were sampled every 15 min up to 180 min; the interval −15 to 0 min was performed in the dark to establish adsorption equilibrium. Three conditions were evaluated: (i) dye + UV (no catalyst), (ii) dye + catalyst (dark), and (iii) dye + catalyst + UV (photocatalysis). The temperature was maintained at ~20 °C. All experiments were conducted at the natural pH of the dye solution without adjustment. Dye concentrations were obtained from the absorbance at 520 nm (RA) using a (Thermo EvolutionTM 60S UV–Vis spectrophotometer, Thermo Fisher Scientific, Waltham, MA, USA).

The degradation percentage, $\%\eta$, was determined using the following equation:

$$\%\eta = \frac{(A_0 - A_t)}{A_0} \times 100 = \frac{(C_0 - C_t)}{C_0} \times 100 \quad (1)$$

where A_0 corresponds to the initial absorbance of the dye mixture and A_t, to the absorbance after t minutes. Both values are related to the initial concentrations, C_0, and the concentration at time t, C_t, which varies according to the Lambert–Beer law [23].

Chemical oxygen demand (COD, dichromate method) was measured before irradiation and after reaction to assess mineralization. Full experimental details (COD protocol) are provided in the Supplementary Materials. The COD calibration curve obtained using potassium hydrogen phthalate (KHP) standards is presented in Figure 2. The relationship between COD and the baseline-corrected absorbance (A_{BC}) follows:

$$\text{COD } [\text{mg } O_2 \cdot L^{-1}] = 138.05 \cdot A_{BC} + 1.4 \quad (2)$$

Detailed calibration data are provided in Table S1 (Supplementary Materials).

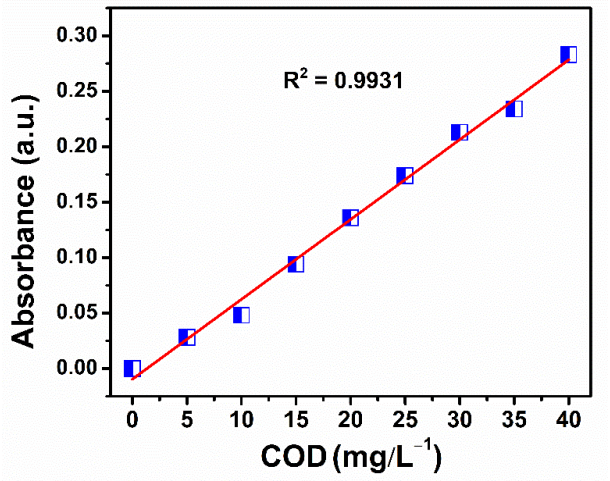

Figure 2. COD calibration curve used for mineralization analysis during RA photodegradation.

The mineralization efficiency of RA was evaluated using the (COD) values determined before and after photocatalytic treatment according to the following equation:

$$\text{Removal RA } (\%) = \frac{COD_0 - COD_t}{COD_0} \times 100 \quad (3)$$

where COD_0 corresponds to the initial COD value of the RA solution and COD_t represents the COD measured after irradiation time t.

3. Results and Discussion

3.1. Physicochemical Analysis of CeO_2

The optical band gap of CeO_2 was estimated from UV–Vis absorption data using the Tauc method. The Tauc relation between the absorption coefficient (α) and the photon energy ($h\nu$) is:

$$\alpha h\nu = B\left(h\nu - E_g\right)^n \quad (4)$$

where B is a constant and n depends on the electronic transition. For CeO_2, a direct allowed transition was assumed (n = 2) [7]. E_g was obtained by linear fitting of the high-energy region of $(\alpha h\nu)^2$ versus $h\nu$ and extrapolation to the energy axis (Figure 3). The resulting optical band gap was ~3.24 eV, consistent with reported values for CeO_2 [1,2].

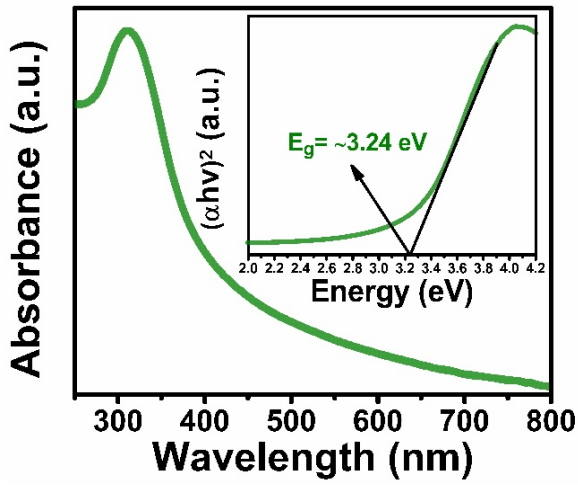

Figure 3. Optical absorption spectrum and Tauc plot of CeO_2.

The XRD pattern of CeO_2 (Figure 4) shows reflections at 2θ = 28.51°, 33.05°, 47.37°, 56.27°, 59.09°, 69.33°, 76.61°, 79.25°, and 88.39°, indexed to the (111), (200), (220), (311), (222), (400), (331), (420), and (422) planes, respectively. These peaks agree with the cubic fluorite structure of CeO_2 nanoparticles (ICSD 98-006-1595) and with previous reports [7,13,14]. The crystallite size D was estimated using the Debye–Scherrer equation:

$$D = \frac{0.9\,\lambda}{\beta\cos\theta} \quad (5)$$

where λ is the wavelength, β is the full width at half maximum (FWHM), and θ is the Bragg's angle expressed in radians. The calculated crystal size was ~14.7 nm.

Additionally, the interplanar distance (d) for the plane (111) was determined by Bragg's equation:

$$d = \frac{n\lambda}{2\sin\theta} \quad (6)$$

The results indicated that the interplanar distance was ~0.31 nm for the plane (111) [14,15].

TEM micrographs in Figure 5 are representative of the CeO_2 samples. Figure 5a shows agglomerates of near-spherical primary crystallites with an average particle

size of ~10.6 nm. XRD analysis yielded a crystallite size of ~14.7 nm, calculated using the Scherrer equation. The slight difference between TEM and XRD values is expected, as XRD estimates coherent crystalline domain size based on diffraction broadening, whereas TEM measures the physical particle size and may reflect size dispersion effects.

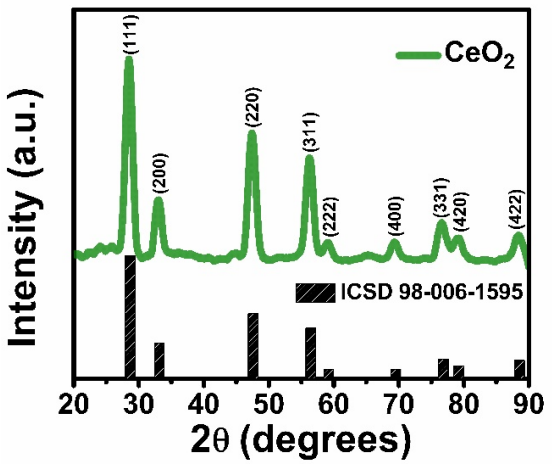

Figure 4. X-ray diffraction pattern of CeO_2 nanoparticles.

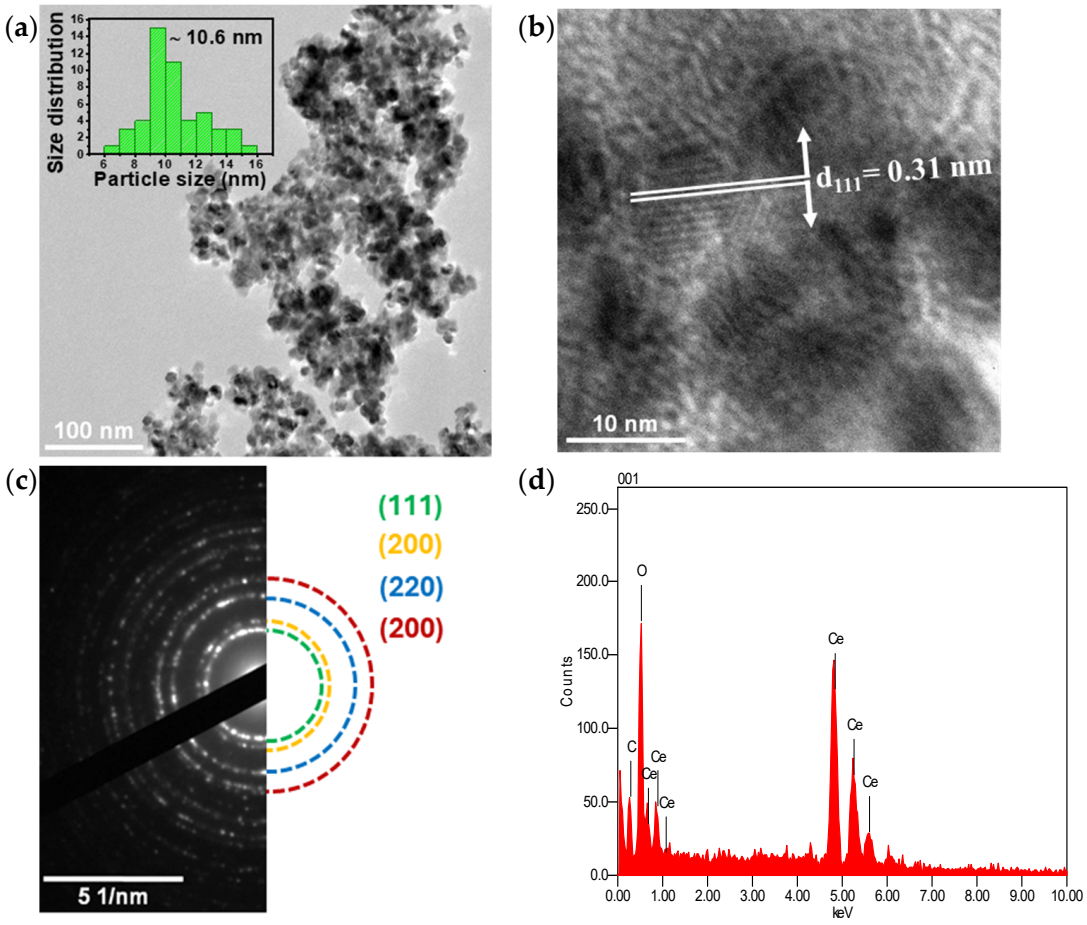

Figure 5. TEM/EDS characterization of CeO_2 nanoparticles: (**a**) low-magnification TEM micrograph; (**b**) HR-TEM lattice fringes; (**c**) SAED ring pattern indexed; (**d**) EDS spectrum.

Figure 5b (HR-TEM) displays lattice fringes with d_{111} = ~0.31 nm, assigned to the (111) planes of fluorite CeO_2 [14,15]. The selected-area electron diffraction (SAED) pattern in Figure 5c exhibits concentric rings indexed, confirming a crystalline nature. The EDS

spectrum (Figure 5d) shows only Ce and O within detection limits; minor C arises from the carbon support.

Textural properties were assessed by N_2 adsorption–desorption isotherms at 77 K (Figure 6). The isotherm exhibits a type IV profile according to the IUPAC classification, confirming mesoporosity [24]. The Brunauer–Emmett–Teller (BET) surface area was 85.27 $m^2 \cdot g^{-1}$, with a total pore volume of 0.27 $cm^3 \cdot g^{-1}$, indicating a mesoporous structure with a high density of accessible surface sites. In CeO_2-based systems, such textural features, together with surface defect chemistry, have been reported to enhance dye adsorption and promote interfacial charge separation and reactive oxygen species generation during photocatalysis [25,26].

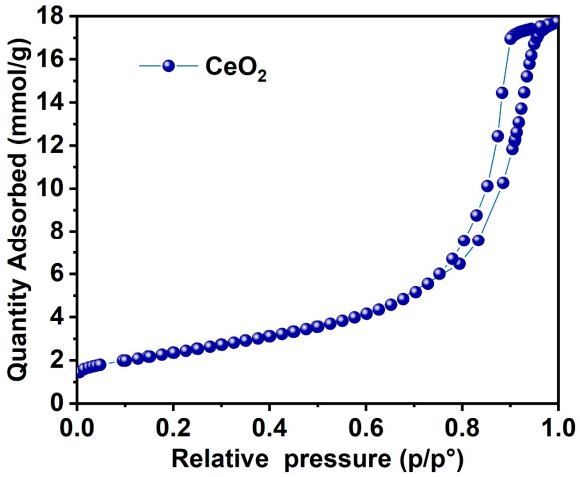

Figure 6. N_2 adsorption–desorption isotherm of CeO_2 nanoparticles.

3.2. Photocatalytic Degradation of RA Dye

In the UV–Vis curves (Figure 7a–c), the main bands of RA (~520 nm) remain essentially unchanged under UV-A without catalyst, confirming negligible photolysis at 365 nm. In the dark with CeO_2, a decrease attributed to dye adsorption on the catalyst surface is observed, consistent with the $-15 \rightarrow 0$ min pre-stage. Only under the CeO_2 + UV-A condition, the bands decrease monotonically to near-baseline, evidencing effective photocatalysis.

Figure 8a,b show the percent-removal for each case and kinetic curves for the UV-A + RA + CeO_2, respectively. The fits follow typical pseudo-first-order degradation kinetics ($\ln(C_0/C_t)$ vs. t), with estimated rate constants k_{RA} = 0.0125 min^{-1}; the half-life was $t_{1/2}$ = ~55 min. At 180 min, with a catalyst loading of 1.0 $g \cdot L^{-1}$ (50 mg in 50 mL), removals of ~90% RA were achieved, consistent with the obtained k value. The contributions estimated at 180 min were as follows: photolysis (UV only) ~6%, adsorption (CeO_2 in the dark, $-15 \rightarrow 0$ min) ~30%; total removal under CeO_2 + UV-A ~90%. The apparent photocatalytic fraction (CeO_2 + UV − UV only) was ~84%, and after subtracting the portion removed by adsorption, the net removal by photocatalysis was ~54%. These results are consistent with the linearity of $\ln(C_0/C_t)$ observed in the kinetic plot for RA dye. The ~30% dark adsorption is consistent with the relatively high BET surface area (85.27 $m^2 \cdot g^{-1}$) and mesoporous structure of the CeO_2 nanoparticles (Figure 6), which provide abundant accessible surface sites. Electrostatic and coordination interactions between the azo (–N=N–) and sulfonate ($–SO_3^-$) groups of Red Amaranth and surface Ce sites likely contribute to this initial adsorption. This phenomenon represents a surface pre-concentration effect rather than chemical degradation, facilitating subsequent photocatalytic oxidation under UV-A irradiation. To further evaluate the extent of mineralization, the chemical oxygen demand (COD) of the RA solution was measured before and after photocatalytic treatment. The COD value decreased from 19.8 mg O_2 L^{-1} to 3.0 mg O_2 L^{-1} after 180 min, corresponding

to a mineralization efficiency of approximately 85%. This result confirms that the decrease in dye absorbance is not solely due to decolorization but also reflects substantial oxidation of the organic structure.

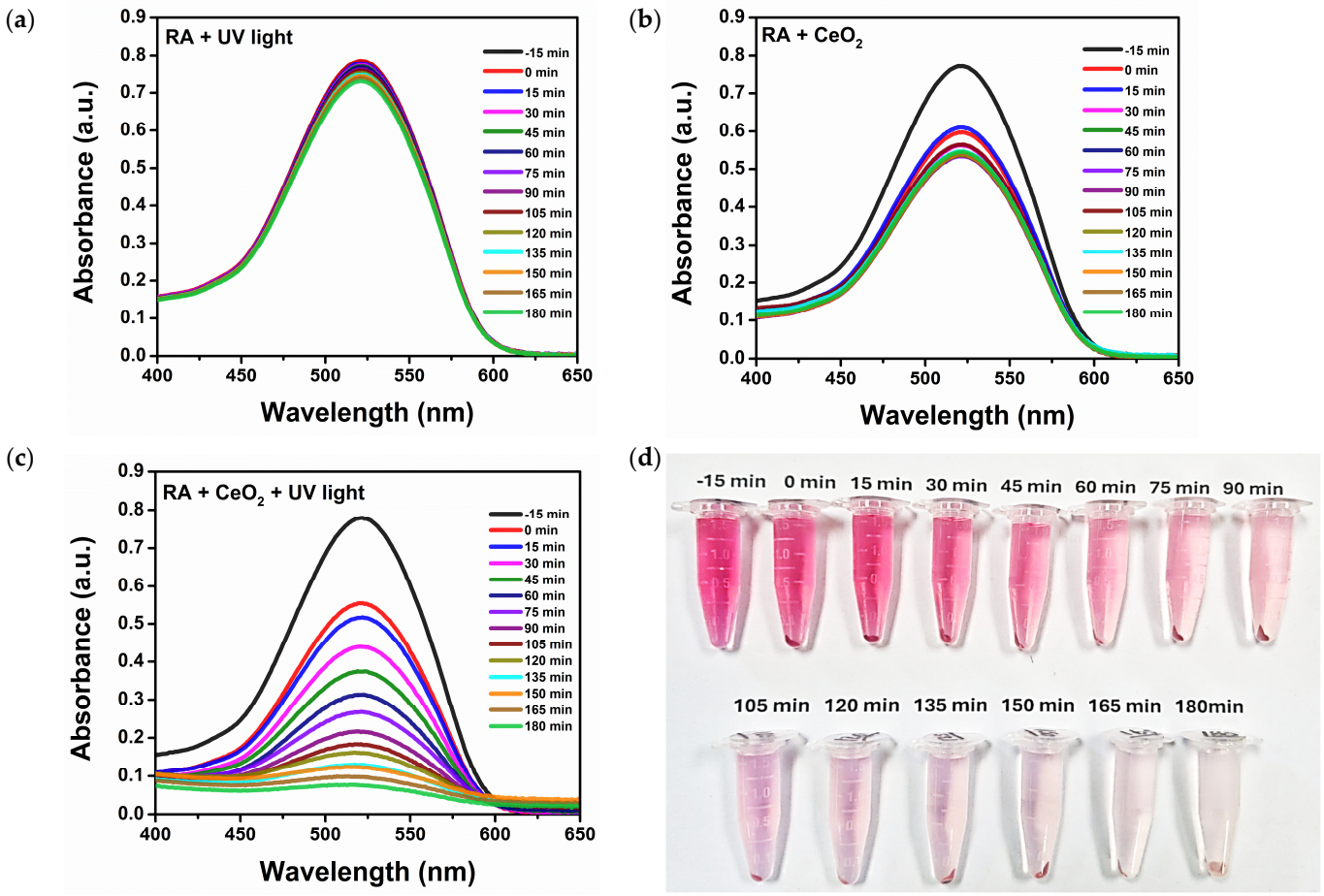

Figure 7. Absorbance spectra for dyes photodegradation of RA (**a**) only UV light, (**b**) with CeO_2 photocatalyst in dark, and (**c**) with CeO_2 photocatalyst and UV light, respectively. (**d**) RA decolorization sequence with CeO_2 + UV.

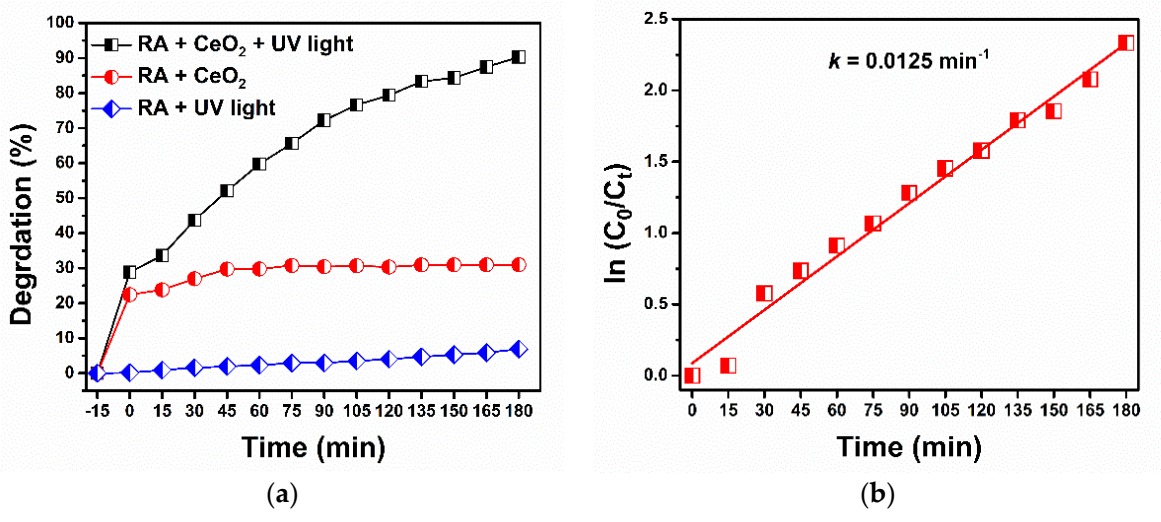

Figure 8. Degradation percentage only UV light, with CeO_2 in dark and photocatalyst (**a**), and kinetic photodegradation curve (**b**).

These photocatalytic results can be rationalized based on the physicochemical properties of the synthesized CeO_2 nanoparticles, which govern the adsorption behavior of the dye molecules and the interfacial charge transfer processes occurring during photocatalysis. In particular, the structural and surface characteristics of the material promote effective interaction between the catalyst surface and the dye molecules, facilitating subsequent photocatalytic oxidation under UV-A irradiation.

The mineralization mechanism of RA mediated by CeO_2 NPs under UV irradiation (365 nm) can be interpreted through three main stages: (i) band-to-band excitation of the oxide (E_g = ~3.0–3.2 eV) with generation of the e^-/h^+ pair, (ii) Ce^{3+}/Ce^{4+} redox dynamics and oxygen vacancies acting as trapping and/or transfer centers that facilitate the activation of ROS, and (iii) cleavage of the azo bond (–N=N–) of the dye, progressive oxidation of aromatic intermediates, and subsequent complete mineralization to CO_2 and H_2O. This process involves the absorption of UV radiation by the CeO_2 nanoparticles, which promotes the excitation of electrons (e^-) from the valence band (VB) to the conduction band (CB), thus generating the e^-/h^+ pair. This process partially reduces Ce^{4+} species in CeO_2-NPs to Ce^{3+} (CeO_{2-x}-NPs), simultaneously creating oxygen vacancies [1,27,28].

The photogenerated h^+ oxidize water and OH^- ions, generating •OH radicals, while conduction band electrons reduce O_2 (dissolved and/or at vacancies) to $•O_2^-$, which protonates to $HO_2•$, contributing to the oxidative attack. The first step on the AR molecule is the cleavage of the azo bond (–N=N–), splitting the dye into two fragments: sulfonated aromatic derivatives such as sulfanilic- and naphthylamine-type species. These intermediates undergo desulfonation processes, favored by •OH radicals, releasing SO_4^{2-} and forming reactive phenolic compounds [29]. In the case of naphthylamine-type derivatives, oxidation occurs with the $–NH_2$ group transiently converted into nitroso/nitro species and subsequently eliminated as NO_2^-/NO_3^-, while the free aromatic position is substituted by –OH, leading to unstable dihydroxylated structures. These species transform into quinonic compounds through oxidative tautomerization, which are highly susceptible to •OH and $•O_2^-$ radical-induced ring-opening reactions, producing low-molecular-weight carboxylic acids such as maleic, oxalic, and formic acids [30,31]. On the other hand, aromatic intermediates undergo rapid desulfonation, yielding sulfonated phenols that are also hydroxylated and fragmented, converging into carboxylic species. Ultimately, both pathways lead to substantial oxidation of the organic structure, as supported by the significant COD reduction observed after irradiation, along with the release of inorganic anions [31].

The central role of CeO_2 NPs is attributed to their ability to recycle Ce^{3+}/Ce^{4+} states, thereby generating radicals in a sustained manner, and to the presence of oxygen vacancies, which reduce the recombination of photogenerated charges and enable an efficient redox cycle. Thus, the photocatalytic process mediated by CeO_2 NPs not only induces decolorization but also promotes extensive oxidative transformation of AR under UV irradiation. The mechanism discussed above is proposed based on the experimental trends observed in this study (adsorption and photolysis controls, kinetic behavior, and COD reduction) together with established photocatalytic AOP pathways reported for azo dyes. The intermediates described are therefore interpreted as plausible species consistent with literature reports.

Table 1 summarizes the photocatalytic results for the RA obtained in this work with CeO_2, along with previously reported data for other metal oxide–based catalysts. It is observed that CeO_2 achieves 69% degradation within 120 min under UV irradiation, which increases to 83.6% in the presence of H_2O_2, with a kinetic constant of 0.0993 min^{-1}, outperforming conventional systems such as TiO_2 + H_2O_2 that report 64% degradation in 100 min [3,20]. Although some TiO_2-based systems can achieve higher degradation efficiencies under optimized conditions (e.g., up to ~97% removal within 90 min, as summarized in Table 1), such performances are often associated with modified catalysts or specific

irradiation conditions. In comparison, the CeO_2 nanoparticles evaluated in this work exhibit competitive photocatalytic activity under relatively simple experimental conditions, including the use of a UV-A LED source and the absence of dopants or composite structures. These findings demonstrate that even in the absence of co-catalysts, CeO_2 exhibits remarkable efficiency. Catalysts such as N-WO_3 achieved complete degradation in 120 min under UV-A/visible radiation [16], while the Fe/TiO_2-NaY and Fe-ZnO systems reached efficiencies close to 98% in less than 100 min [17,19]. Similarly, advanced heterostructures such as Ag/N-g-C_3N_4 report nearly complete degradation (99.7%) in only 30 min [32]. Nevertheless, it should be noted that most of these reports are focused on traditional materials such as TiO_2 and ZnO or on more recent heterostructures, whereas studies on RA photocatalysis using CeO_2 remain very limited, hindering direct comparisons and underscoring the relevance of the present work. The performance observed for CeO_2 can be attributed to its ability to generate reactive oxygen species through the Ce^{3+}/Ce^{4+} redox cycles, reflecting its potential as a promising photocatalyst. This comparison not only positions CeO_2 as a competitive material against classical oxides but also emphasizes the need to further explore its application in the degradation of emerging contaminants.

Table 1. Comparative performance of CeO_2-based photocatalysts for RA under UV irradiation.

Photocatalyst	Light Source	Power (W)	Dye (C_0)	V (mL)	Catalyst (mg)	Load ($g \cdot L^{-1}$)	% η (Time)	k (min^{-1})	% COD	Ref.
CeO_2 NPs	UV	—	Amaranth 20 $mg \cdot L^{-1}$	50	50	1.0	69% (120 min, without H_2O_2); 83.6% (120 min, with H_2O_2)	0.0993	—	[20]
TiO_2 + H_2O_2	UV-C lamp	6	Amaranth (0.01 M)	—	—	—	64% (100 min)	—	—	[3]
N-WO_3	UV-A/Visible		Amaranth 25 $mg \cdot L^{-1}$	—	1000	1.0	100% (120 min)	—	—	[16]
ZnS (QDs)	UV lamp	8	Amaranth 250–500 $mg \cdot L^{-1}$	—	—	variable	85% (120 min)	—	—	[4]
TiO_2	—	—	Amaranth 30 $mg \cdot L^{-1}$	200	110	—	97.14% (90 min)	0.069	—	[18]
Fe-ZnO	Fluorescent lamp	6	Amaranth	—	—	—	98% (80 min)	0.0114	—	[19]
$MnFe_2O_4$@ZnO	UV-C lamp	—	Amaranth, 20 $mg \cdot L^{-1}$	250	—	—	60% (240 min)	3.94×10^{-3}	34.1%	[33]
TiO_2-NPs	UV lamp	11	Amaranth, 242 $mg \cdot L^{-1}$	10	3	0.3	~85–90% (90 min)	0.0671	—	[34]
Ag/N-g-C_3N_4	Xe lamp	300	Amaranth —	—	—	—	99.7% (30 min)	—	—	[32]
CeO_2 nanoparticles	UV-A LED	100	Red Amaranth 20 $mg \cdot L^{-1}$	50	50	1.0	RA ~90% (180 min)	0.0125	85%	This Work

In summary, with moderate catalyst loadings (1.0 $g \cdot L^{-1}$), a 365 nm LED source, and thermal control, the CeO_2 obtained here exhibits high conversions and competitive kinetics compared with recent references, without dopants or supports. Moreover, the COD results (before/after) confirm dye mineralization, demonstrating that the time-dependent decrease in absorbance is not due solely to decolorization.

4. Conclusions

CeO_2 nanoparticles synthesized by controlled precipitation exhibited effective photocatalytic degradation of Red Amaranth under UV-A LED irradiation (365 nm, 1.0 $g \cdot L^{-1}$, ~20 °C), achieving ~90% decolorization within 180 min and following pseudo-first-order kinetics (k_{RA} = 0.0125 min^{-1}). Control experiments confirmed negligible photolysis and a ~30% dark adsorption contribution, which is consistent with the relatively high BET

surface area (85.27 $m^2 \cdot g^{-1}$) and mesoporous structure of the nanoparticles. COD measurements (from 19.8 to 3.0 mg $O_2 \cdot L^{-1}$) indicate substantial oxidation of the organic structure beyond chromophore bleaching.

The photocatalytic performance is attributed to the synergistic role of surface adsorption, Ce^{3+}/Ce^{4+} redox cycling, and oxygen vacancy-mediated reactive oxygen species generation, establishing a clear structure–activity relationship. Overall, these findings position CeO_2 as a promising UV-responsive oxide for azo dye degradation under controlled conditions.

Further investigations involving reactive species identification, TOC analysis, catalyst stability assessment, and evaluation under complex water matrices will contribute to a more comprehensive understanding of the mechanistic pathways and practical applicability of this system.

Supplementary Materials: The following supporting information can be downloaded at: https://www.mdpi.com/article/10.3390/reactions7020022/s1. Table S1. COD calibration data (KHP): absorbance, baseline-corrected absorbance (Abc), and calculated COD; includes RA samples before (−15 min) and after (180 min) photodegradation. Figure S1. Photograph of the photocatalytic reactor setup used in this study, showing the UV-A LED source (365 nm), reactor configuration, and magnetic stirring system.

Author Contributions: Conceptualization, J.C.-S. and E.E.-M.; investigation, J.C.-S. and E.E.-M.; methodology, E.E.-M., J.S.-C. and E.P.-P.; writing—original draft preparation, J.C.-S., E.E.-M., B.V.-S. and E.P.-P.; writing—review and editing, J.S.-C., B.V.-S., E.B.-P., R.G.-B. and E.P.-P.; visualization, J.C.-S. and B.V.-S.; supervision, J.C.-S. and B.V.-S.; project administration, J.C.-S. and B.V.-S.; funding acquisition, J.C.-S., B.V.-S. and E.B.-P. All authors have read and agreed to the published version of the manuscript.

Funding: This research was funded by the program No. CBF-2025-I-4009, "Ciencia Básica y de Frontera 2025" CBF2025, SECIHTI, and Program No. 317330 FOP02 CONACYT. Jhonathan Castillo-Saenz was supported in part by a doctoral grant from the Ministerio de Ciencia, Tecnología e Innovación (Minciencia885/2020) y Colfuturo—Colombia.

Data Availability Statement: The data presented in this study are available from the corresponding author upon reasonable request.

Acknowledgments: We thank the Instituto de Ingeniería, Universidad Autónoma de Baja California, and acknowledge the financial support of SECIHTI.

Conflicts of Interest: The authors declare that they have no known competing financial interests or personal relationships that could have appeared to influence the work reported in this paper.

References

1. Kusmierek, E. A CeO_2 Semiconductor as a Photocatalytic and Photoelectrocatalytic Material for the Remediation of Pollutants in Industrial Wastewater: A Review. *Catalysts* **2020**, *10*, 1435. [CrossRef]
2. Trandafilović, L.V.; Jovanović, D.J.; Zhang, X.; Ptasińska, S.; Dramićanin, M.D. Enhanced Photocatalytic Degradation of Methylene Blue and Methyl Orange by ZnO:Eu Nanoparticles. *Appl. Catal. B* **2017**, *203*, 740–752. [CrossRef]
3. Gupta, V.K.; Jain, R.; Mittal, A.; Saleh, T.A.; Nayak, A.; Agarwal, S.; Sikarwar, S. Photo-Catalytic Degradation of Toxic Dye Amaranth on TiO_2/UV in Aqueous Suspensions. *Mater. Sci. Eng. C* **2012**, *32*, 12–17. [CrossRef]
4. Correa-Vargas, K.D.; Luciano-Velázquez, J.; Nash-Montes, V.I.; Bailón-Ruiz, S.J. Photocatalytic Activity of Zinc Sulfide Quantum Dots on Amaranth Dye. *MRS Adv.* **2022**, *7*, 295–299. [CrossRef]
5. Yan, Y.-Q.; Wu, Y.-Z.; Wu, Y.-H.; Weng, Z.-L.; Liu, S.-J.; Liu, Z.-G.; Lu, K.-Q.; Han, B. Recent Advances of CeO_2-Based Composite Materials for Photocatalytic Applications. *ChemSusChem* **2024**, *17*, e202301778. [CrossRef]
6. Fauzi, A.A.; Jalil, A.A.; Hassan, N.S.; Aziz, F.F.A.; Azami, M.S.; Hussain, I.; Saravanan, R.; Vo, D.V.N. A Critical Review on Relationship of CeO_2-Based Photocatalyst Towards Mechanistic Degradation of Organic Pollutant. *Chemosphere* **2022**, *286*, 131651. [CrossRef] [PubMed]

7. Herzog, A.E.; Michael, T.J.; Dunkelburger, A.D.; Johannes, M.D.; Rolison, D.R.; DeSario, P.A.; Novak, T.G. Nanostructured CeO_2 Photocatalysts: Optimizing Surface, Morphology, and Visible-Light Absorption. In *Proceedings of the AIChE Annual Meeting*; American Institute of Chemical Engineers: Orlando, FL, USA, 2019.
8. El-Khawaga, A.M.; Tantawy, H.; Elsayed, M.A.; El-Mageed, A.I.A.A. Development of Novel Reduced Graphene Oxide/Metalloporphyrin Nanocomposite with Photocatalytic and Antimicrobial Activity for Potential Wastewater Treatment and Medical Applications. *Sci. Rep.* **2024**, *14*, 27916. [CrossRef] [PubMed]
9. Rizki, I.N.; Inoue, T.; Chuaicham, C.; Shenoy, S.; Srikhaow, A.; Sekar, K.; Sasaki, K. Fabrication of Reduced Ag Nanoparticle Using Crude Extract of Cinnamon Decorated on ZnO as a Photocatalyst for Hexavalent Chromium Reduction. *Catalysts* **2023**, *13*, 265. [CrossRef]
10. Chen, C.; Shenoy, S.; Chuaicham, C.; Trakulmututa, J.; Tian, Q.; Zhang, H.; Sasaki, K. Enhancing photocatalytic efficiency: Geopolymer-supported TiO_2 composites for sustainable organic pollutant degradation. *Opt. Mater.* **2024**, *150*, 115165. [CrossRef]
11. Xie, W.; Liu, G.; Liu, Y.; Bai, Y.; Liao, Y.; Li, T.; Wang, C.; Chang, S.; Hu, J. Multidimensional TiO_2 photocatalysts for the degradation of organic dyes in wastewater treatment. *J. Porous Mater.* **2024**, *31*, 1655–1681. [CrossRef]
12. Ai, X.; Yan, S.; Lin, C.; Lu, K.; Chen, Y.; Ma, L. Facile Fabrication of Highly Active CeO_2@ZnO Nanoheterojunction Photocatalysts. *Nanomaterials* **2023**, *13*, 1371. [CrossRef] [PubMed]
13. Ray, S.K.; Dahal, R.; Ashie, M.D.; Alonzo, S.M.M.; Binod Raj, K.C.; Bastakoti, B.P. Recent Progress on Cerium Oxide-Based Nanostructures for Energy and Environmental Applications. *Adv. Energy Sustain. Res.* **2025**, *6*, 2500022. [CrossRef]
14. Castillo-Saenz, J.; Salomón-Carlos, J.; Beltrán-Partida, E.; Valdez-Salas, B. Eco-Friendly Synthesis of Cerium Oxide Nanoparticles from *Lycium cooperi*. *Reactions* **2025**, *6*, 14. [CrossRef]
15. Bi, H.; Zhang, L.X.; Xing, Y.; Zhang, P.; Chen, J.J.; Yin, J.; Bie, L.J. Morphology-Controlled Synthesis of CeO_2 Nanocrystals and Their Facet-Dependent Gas Sensing Properties. *Sens. Actuators B Chem.* **2021**, *330*, 129374. [CrossRef]
16. Sudrajat, H.; Babel, S. Rapid Photocatalytic Degradation of the Recalcitrant Dye Amaranth by Highly Active N-WO_3. *Environ. Chem. Lett.* **2016**, *14*, 243–249. [CrossRef]
17. Alwash, A.H.; Abdullah, A.Z.; Ismail, N. Zeolite Y Encapsulated with Fe-TiO_2 for Ultrasound-Assisted Degradation of Amaranth Dye in Water. *J. Hazard. Mater.* **2012**, *233–234*, 184–193. [CrossRef]
18. Naik, A.P.; Salkar, A.V.; Majik, M.S.; Morajkar, P.P. Enhanced Photocatalytic Degradation of Amaranth Dye on Mesoporous Anatase TiO_2: Evidence of C–N, N=N Bond Cleavage and Identification of New Intermediates. *Photochem. Photobiol. Sci.* **2017**, *16*, 1126–1138. [CrossRef]
19. Warangule, A.; Balgude, S.; Nehare, G.; Waghmode, S.; Jagtap, R. Investigating the Photocatalytic Degradation of Amaranth Dye in Water Environment Using Visible Light-Activated Fe-Doped ZnO Nanoparticles. *Phys. Status Solidi A* **2023**, *220*, 2300417. [CrossRef]
20. Bassi, A.; Qanungo, K.; Hasan, I.; Alshayiqi, A.A.; Ababtain, A.S.; Alharthi, F.A. CuO Nanorods Immobilized Agar-Alginate Biopolymer: A Green Functional Material for Photocatalytic Degradation of Amaranth Dye. *Polymers* **2023**, *15*, 553. [CrossRef]
21. Yao, N.; Liu, Z.; Chen, Y.; Zhou, Y.; Xie, B. A Novel Thermal Sensor for the Sensitive Measurement of Chemical Oxygen Demand. *Sensors* **2015**, *15*, 20501–20510. [CrossRef]
22. U.S. Environmental Protection Agency (EPA). *Oxygen Demand, Chemical (COD), Colorimetric, Dichromate Oxidation—Interferences and Limitations*; Method I-3561-85; U.S. EPA: Washington, DC, USA, 1985.
23. Mayerhöfer, T.G.; Pahlow, S.; Popp, J. The Bouguer-Beer-Lambert Law: Shining Light on the Obscure. *ChemPhysChem* **2020**, *21*, 2029–2046. [CrossRef]
24. Thommes, M.; Kaneko, K.; Neimark, A.V.; Olivier, J.P.; Rodríguez-Reinoso, F.; Rouquerol, J.; Sing, K.S.W. Physisorption of gases, with special reference to the evaluation of surface area and pore size distribution (IUPAC Technical Report). *Pure Appl. Chem.* **2015**, *87*, 1051–1069. [CrossRef]
25. Ahamed, M.; Mansoor Ali, S.; Lateef, A.; Dotto, G.L.; Alhadlaq, H.A. Oxygen-Vacancy Engineering and Junction Design in CeO_2 Nanomaterials for Photocatalysis and Antibacterial Action: A Review. *Results Eng.* **2025**, *28*, 108076. [CrossRef]
26. Lawrence, N.J.; Brewer, J.R.; Wang, L.; Wu, T.-S.; Wells-Kingsbury, J.; Ihrig, M.M.; Wang, G.; Soo, Y.-L.; Mei, W.-N.; Cheung, C.L. Defect Engineering in Cubic Cerium Oxide Nanostructures for Catalytic Oxidation. *Nano Lett.* **2011**, *11*, 2666–2671. [CrossRef] [PubMed]
27. Sinha, A.; Sahu, S.K.; Biswas, S.; Ghorai, T.K. Synthesis of CeO_2/ZrO_2/ZnO Nano Alloy Oxide and Investigation of Photocatalysis of Naphthol Orange under Sunlight. *RSC Adv.* **2023**, *13*, 22029–22042. [CrossRef]
28. Murugadoss, G.; Kumar, D.D.; Kumar, M.R.; Venkatesh, N.; Sakthivel, P. Silver Decorated CeO_2 Nanoparticles for Rapid Photocatalytic Degradation of Textile Rose Bengal Dye. *Sci. Rep.* **2021**, *11*, 1080. [CrossRef]
29. Karkmaz, M.; Puzenat, E.; Guillard, C.; Herrmann, J.M. Photocatalytic Degradation of the Alimentary Azo Dye Amaranth: Mineralization of the Azo Group to Nitrogen. *Appl. Catal. B* **2004**, *51*, 183–194. [CrossRef]
30. Khitab, F.; Jan, M.R.; Shah, J. Sonophotocatalytic Degradation of Aqueous Acid Red 27 and Direct Violet 51 Using Copper Impregnated Al_2O_3. *Desalin. Water Treat.* **2019**, *137*, 381–394. [CrossRef]

31. Ananthi, U.; Saral, A.M. Morphology Controlled-Surfactant Free Plant-Mediated Synthesis of $BiVO_4$ and Its Dye Degradation Property. *Biomass Convers. Biorefin.* **2025**, *15*, 21203–21226. [CrossRef]
32. Wang, S.; Zheng, Z.; Zhao, Y.; Wang, H. Boosting Photocatalytic Activity of g-C_3N_4 Through Dual Modification: N-Doping and Ag NPs Synergy for Rapid Azo Dye Degradation with Mechanistic Insights. *J. Inorg. Organomet. Polym. Mater.* **2025**, *36*, 97–110. [CrossRef]
33. Lopez Medina, J.A.; Domínguez, D.; Pizá, P.; Liu, G.; Velez, C.; Reyes Gómez, F.; Farías, M.H.; Caudillo-Flores, U.; Soto Herrera, G.; Tiznado, H.; et al. Magnetic Photocatalyst Nanocomposite Based on $MnFe_2O_4$@ZnO for AZO Dye Degradation. *ACS Omega* **2025**, *10*, 17595–17610. [CrossRef]
34. Rehman, R.; Zaman, W.U.; Raza, A.; Noor, W.; Batool, A.; Maryem, H. Photocatalytic Degradation of Alizarin Red S, Amaranth, Congo Red, and Rhodamine B Dyes Using UV Light Modified Reactor and ZnO, TiO_2, and SnO_2 as Catalyst. *J. Chem.* **2021**, *2021*, 6655070. [CrossRef]